

# Thermal X-Ray Emission from Shocked Ejecta in Type Ia Supernova Remnants II: Parameters Affecting the Spectrum

Carles Badenes<sup>1</sup>, Kazimierz J. Borkowski<sup>2</sup> and Eduardo Bravo<sup>3,4</sup>

## ABSTRACT

The supernova remnants left behind by Type Ia supernovae provide an excellent opportunity for the study of these enigmatic objects. In a previous work, we showed that it is possible to use the X-ray spectra of young Type Ia supernova remnants to explore the physics of Type Ia supernovae and identify the relevant mechanism underlying these explosions. Our simulation technique is based on hydrodynamic and nonequilibrium ionization calculations of the interaction of a grid of Type Ia explosion models with the surrounding ambient medium, coupled to an X-ray spectral code. In this work we explore the influence of two key parameters on the shape of the X-ray spectrum of the ejecta: the density of the ambient medium around the supernova progenitor and the efficiency of collisionless electron heating at the reverse shock. We also discuss the performance of recent 3D simulations of Type Ia SN explosions in the context of the X-ray spectra of young SNRs. We find a better agreement with the observations for Type Ia supernova models with stratified ejecta than for 3D deflagration models with well mixed ejecta. We conclude that our grid of Type Ia supernova remnant models can improve our understanding of these objects and their relationship to the supernovae that originated them.

---

<sup>1</sup>Department of Physics and Astronomy, Rutgers University, 136 Frelinghuysen Rd., Piscataway NJ 08854-8019; badenes@physics.rutgers.edu

<sup>2</sup>Department of Physics, North Carolina State University, Box 8202, Raleigh NC 27965-8202; kborkow@unity.ncsu.edu

<sup>3</sup>Departament de Física i Enginyeria Nuclear, Universitat Politècnica de Catalunya, Diagonal 647, Barcelona 08028, Spain; eduardo.bravo@upc.es

<sup>4</sup>Institut d'Estudis Espacials de Catalunya, Campus UAB, Facultat de Ciències. Torre C5. Bellaterra, Barcelona 08193, Spain

*Subject headings:* hydrodynamics — ISM — nuclear reactions, nucleosynthesis, abundances, — supernova remnants — supernovae:general — X-rays:ISM

## 1. INTRODUCTION

The advent of modern X-ray observatories such as *Chandra* and *XMM-Newton* has produced a spectacular increase in both the quantity and the quality of the observations of Type Ia supernova remnants (SNRs). Yet, these excellent observations have led only to a modest improvement in our knowledge of the physics of Type Ia supernovae (SNe). Important issues such as the nature of the progenitor systems, the last stages of their evolution prior to the SN explosion or the physical mechanism behind the explosion itself still remain obscure (see Hillebrandt & Niemeyer 2000; Branch & Khokhlov 1995, for reviews). In a recent paper (Badenes et al. 2003, henceforth Paper I), we examined the prospects for the identification of the explosion mechanism in Type Ia SNe through the analysis of the X-ray spectra of young SNRs. We assembled a grid of Type Ia SN explosion models, simulated their interaction with a uniform ambient medium (AM) and calculated the predicted X-ray spectra from the ensuing SNRs. The calculated X-ray SNR spectra varied dramatically from model to model, demonstrating that it is possible to use young Type Ia SNRs to probe the details of the Type Ia SN explosion mechanism.

In this paper, we expand the results that were introduced in Paper I. Our objective is to examine the relationship between Type Ia SN explosions and the X-ray spectra of their SNRs within the framework of hydrodynamic, ionization, and spectral simulations. By comparing our models with observations, we aim at improving our understanding of both Type Ia SNe and young, ejecta-dominated SNRs. In § 2, we review the simulation scheme used in Paper I, and we discuss the influence of two important parameters which we had not hitherto explored: the amount of collisionless electron heating at the reverse shock and the density of the uniform AM that interacts with the ejecta. In § 3 we examine the performance of recent 3D Type Ia SN explosion models in the context of SNRs, and we discuss the ability of these 3D models to reproduce the fundamental properties of the X-ray spectra of Type Ia SNRs. Our conclusions are presented in § 4. In order to facilitate the comparison between our models and X-ray observations of SNRs, we have generated a library of synthetic spectra. This library is presented and discussed in the Appendix. In a forthcoming paper (Badenes et al., in preparation), we will make a detailed comparison between our models and the X-ray spectrum of the Tycho SNR.

## 2. PARAMETERS AFFECTING THE X-RAY SPECTRUM

### 2.1. From SN to SNR: the Simulation Scheme

Although the X-ray spectra of young Type Ia SNRs contain much information about the structure and composition of the material ejected by the SNe that originated them, this information is generally difficult to extract. The ejecta material consists almost entirely of heavy elements that are impulsively heated to X-ray emitting temperatures as the reverse shock propagates inwards in the reference frame of the expanding ejecta. The propagation of the reverse shock is in turn intimately related to the density structure of the ejecta, which results in an intricate dynamical behavior of the SNR early in its evolution (see Dwarkadas & Chevalier 1998). If there is a significant degree of stratification in the elemental composition of the ejecta, different chemical elements are shocked at different evolutionary times, after different periods of free expansion, and therefore emit X-rays under different physical conditions. This results in a very complex spectrum, which is hard to model and interpret.

The approach taken in Paper I was based on a grid of 1D Type Ia SN explosion models that included all the mechanisms currently under debate for the single degenerate Type Ia SN scenario: deflagrations, delayed detonations, pulsating delayed detonations and sub-Chandrasekhar explosions. The dynamics of the interaction of each explosion model with a uniform ambient medium (AM) of density  $\rho_{AM} = 10^{-24} \text{ g} \cdot \text{cm}^{-3}$  was followed with a 1D hydrodynamic code. The dynamic evolution of each fluid element in the shocked ejecta (i.e., the time evolution of density  $\rho$  and specific internal energy per unit mass  $\varepsilon$ ), together with its chemical composition as determined by the SN explosion model, were used as the input to ionization calculations. These calculations included the interactions between ions and electrons in the shocked plasma, and they provided time-dependent nonequilibrium ionization (NEI) states and electron temperature. Using these ionization states and electron temperatures, spatially integrated synthetic X-ray spectra were generated with a spectral code by adding the weighted contributions from each fluid element in the shocked ejecta. For a more detailed explanation, see Paper I and the references therein.

Within this simulation scheme, the X-ray spectrum from the shocked ejecta is determined by: (1) the density and chemical composition profiles of the SN ejecta from the explosion model, (2) the age of the SNR, (3) the amount of collisionless electron heating at the reverse shock, and (4) the density of the uniform AM. In Paper I, we analyzed the importance of (1) and (2); the impact of (3) and (4) is the focus of this Section.

## 2.2. Collisionless Electron Heating at the Reverse Shock

The unknown efficiency of collisionless electron heating in SNR shocks is one of the main uncertainties affecting the calculated X-ray spectra of SNRs. Direct application of the Rankine-Hugoniot relations at the shock front yields

$$T_p = \frac{3m_p v_s^2}{16k} \quad (1)$$

for each population of particles  $p$ , where  $m_p$  is the particle mass,  $v_s$  is the shock velocity and  $k$  is Boltzmann’s constant. Because of the large difference between electron and ion masses, the electrons are expected to be much colder than the ions, and the quotient of postshock specific internal energies defined as

$$\beta \equiv \frac{\varepsilon_{e,s}}{\varepsilon_{i,s}} = \frac{\overline{Z}_s T_{e,s}}{T_{i,s}} \quad (2)$$

is expected to be close to 0, where  $\overline{Z}_s$  is the preshock ionization state (i.e., the number of free electrons per ion in the unshocked ejecta). However, Cargill & Papadopoulos (1988) argued that plasma waves can redistribute energy among cold electrons and hot ions at the shock, bringing the value of  $\beta$  close to  $\overline{Z}_s$  (for a discussion of collisionless electron heating see Laming 2000).

So far, the observational evidence hints at a decreasing level of thermal equilibration with increasing shock speeds or Mach numbers in the forward shocks of SNRs (see Rakowski et al. 2003, and references therein). In the forward shock of Tycho, Ghavamian et al. (2001) found a value of  $T_e/T_i \leq 0.1$  by analyzing the optical Balmer emission, while Vink et al. (2003) estimated a much lower value at the forward shock of SN 1006 from X-ray observations. The only constraint on the value of  $\beta$  in the reverse shock of a young Type Ia SNR comes from the absorbed spectrum of the Schweizer and Middleditch star behind SN 1006, where the amount of thermal energy deposited in the electrons was found to be negligible (Hamilton et al. 1997). The model spectra presented in Paper I were calculated assuming no collisionless electron heating at the reverse shock, effectively setting  $\beta$  to the lowest possible value,  $\beta_{min} = \overline{Z}_s \cdot m_e/\overline{m}_i$ , where  $\overline{m}_i$  is the average ion mass in a fluid element. It is clear from the works cited above that, while full thermal equilibration between ions and electrons at the shock (i.e.,  $\beta = \overline{Z}_s$ ) is not compatible with the observations, values of  $\beta$  larger than  $\beta_{min}$  cannot be excluded.

The effect of varying amounts of collisionless electron heating at the forward shock on the X-ray spectrum emitted by the shocked AM of SNRs in the Sedov stage was discussed in Borkowski et al. (2001); here, we shall analyze the impact of a small (but nonzero) amount

of collisionless electron heating at the reverse shock on the properties of the shocked ejecta. We will illustrate this effect using a delayed detonation model as an example. Of all the classes of one-dimensional Type Ia explosion models, delayed detonations have been the most successful in reproducing the light curves and spectra of Type Ia SNe (Höflich & Khokhlov 1996), and therefore it is of much interest to analyze the details of the X-ray emission that these models predict for Type Ia SNRs. Within the delayed detonations, we chose model DDTe because it has the largest amount of intermediate mass elements (Si, S, etc.) in the ejecta. This should make it easier to estimate the effects that collisionless electron heating at the reverse shock has on the prominent X-ray lines from these elements.

Figure 1 shows the shocked ejecta of model DDTe for a uniform AM of density  $\rho_{AM} = 10^{-24} \text{ g} \cdot \text{cm}^{-3}$ , 430 yr after the explosion (the age of the Tycho SNR). The electron heating and plasma ionization processes in the shocked ejecta have been calculated for  $\beta = \beta_{min}$ , 0.01, and 0.1. The unshocked ejecta were assumed to be singly ionized in all cases. As discussed in Paper I, the interaction of ejecta with the AM leads to the formation of density structures within the shocked ejecta, which strongly affect the distributions of ionization states (represented here by the average ion charge  $\bar{Z}$ ), electron temperatures  $T_e$ , and ionization timescales ( $\tau = \int n_e dt$ ). Together with the chemical composition profile of the ejecta, these distribution functions determine the spectral properties of each element, and ultimately the shape of the emitted X-ray spectrum. An important feature of the shocked ejecta is the pronounced density peak towards the contact discontinuity (CD) that appears in all Type Ia SNR models (see Paper I and Dwarkadas & Chevalier 1998).

In the case with no collisionless heating ( $\beta = \beta_{min}$ ), the electron temperature profile rises monotonically from the reverse shock to the CD, as internal energy is gradually redistributed from the hot ions to the cold electrons through Coulomb collisions. The electron temperature profile peaks at the CD, where the fluid elements have been shocked for the longest time and have the highest density (the rate at which the ion and electron temperatures equilibrate in the shocked ejecta scales with  $\rho$ , see eq. 1 in Paper I). Increasing the value of  $\beta$  makes the electrons just behind the reverse shock hotter, but the electron temperature drops as numerous cold electrons are liberated in the ongoing ionization process and the total internal energy in the electrons is redistributed among more particles. For  $\beta = 0.01$ , the electron temperature profile eventually relaxes to the profile obtained without any collisionless heating at the reverse shock, but in the  $\beta = 0.1$  case there is a significant residual temperature excess even in the outermost ejecta layers. The average ionization state and ionization timescale become severely affected only for  $\beta \geq 0.1$ , when the electrons reach extremely high ( $\sim 10^9$  K) temperatures behind the reverse shock. The ionization process is less efficient at these extreme temperatures, leading to lower mean ion charges and ionization timescales in the shocked ejecta.

The significance of this modification in the electron temperature profile is better understood when viewed in the context of the stratification that is inherent to 1D Type Ia SN explosion models. In the case of DDTe, as in all delayed detonation models, the inner ejecta layers are dominated by Fe and Ni, surrounded by a region rich in intermediate mass elements (mostly Si and S, but also Ar, Ca, and others), with O dominating the outermost ejecta layers. In Figure 1, this stratified structure has been represented schematically in panel b. In this example, the increase in  $T_e$  caused by collisionless electron heating at the reverse shock affects primarily the Fe-rich ejecta layers at this age. In terms of the emission measure-averaged electron temperature for each element X,  $\langle T_e \rangle_X$ , increasing the value of  $\beta$  effectively reverses the approximate ordering in  $T_e$  of the ejecta elements that is maintained throughout the evolution of the SNR. This is illustrated in Figure 2, which can be contrasted with Figure 5 in Paper I.

In all the calculations presented here and in Paper I,  $\overline{Z}_s$  has been set to 1, which is generally a good approximation for NEI plasmas in SNRs. Photoionization by UV starlight or by X-rays emitted by the shocked material in the SNR could raise  $\overline{Z}_s$ , but only by a factor of 3–4 (see Hamilton & Fesen 1988). After the shock, the heavy element plasma ionizes rapidly, and the values of  $\overline{Z}(t)$  in fluid elements that started with different  $\overline{Z}_s$  will converge over time. Due to this, the postshock X-ray emission is generally insensitive to moderate variations in the preshock ionization. In the presence of collisionless electron heating, increasing  $\overline{Z}_s$  for a fixed value of  $\beta$  raises the number of ‘hot’ electrons and decreases their temperature in the same proportion. X-ray spectra, however, are sensitive mostly to the total internal energy transferred to the electrons at the shock and to the final electron temperature, and not so much to how the internal energy is distributed among the electrons. For all the values of  $\overline{Z}_s$ , the final electron temperature is similar because the final value of  $\overline{Z}$  is very similar. In view of this, we do not expect significant deviations from the results presented here for  $\overline{Z}_s > 1$  at a fixed value of  $\beta$ .

### 2.3. The Ambient Medium Density

The density of the AM affects the spectral properties of the elements in the shocked ejecta in a dramatic way. This is due to two closely related effects: the acceleration of all the collisional plasma processes in denser media on one hand and the scaling of the hydrodynamic models with  $\rho_{AM}$  on the other hand (see section 4.1 in Paper I for a discussion of the hydrodynamic scaling).

These effects are illustrated in Figures 3 and 4, which display the structure of the shocked ejecta of model DDTe at an age of 430 yr after the explosion, for a uniform AM

of  $\rho_{AM} = 5 \cdot 10^{-24} \text{g} \cdot \text{cm}^{-3}$  and  $\rho_{AM} = 2 \cdot 10^{-25} \text{g} \cdot \text{cm}^{-3}$ , respectively. These simulations are also shown for  $\beta = \beta_{min}$ , 0.01, and 0.1 to facilitate comparison with Figure 1. As a result of the scaling laws mentioned in Paper I, a SNR in a denser AM will be in a more evolved evolutionary stage at any given time, and vice versa – note how the reverse shock has not reached the Fe-dominated region of the ejecta at  $t = 430$  yr for  $\rho_{AM} = 2 \cdot 10^{-25} \text{g} \cdot \text{cm}^{-3}$ . The mean ionization state in the shocked ejecta, which peaks at  $\bar{Z} \simeq 10$  in the outermost Si-dominated layers for  $\rho_{AM} = 10^{-24} \text{g} \cdot \text{cm}^{-3}$ , rises as high as  $\bar{Z} \simeq 15$  for  $\rho_{AM} = 5 \cdot 10^{-24} \text{g} \cdot \text{cm}^{-3}$  in the same region, but only reaches  $\bar{Z} \simeq 6$  for  $\rho_{AM} = 2 \cdot 10^{-25} \text{g} \cdot \text{cm}^{-3}$ . These differences in the mean ionization state correspond to differences in the ionization timescales of roughly an order of magnitude throughout the shocked ejecta for each factor 5 increase in  $\rho_{AM}$ . The electron temperature profiles are affected as well, although only by a factor of  $\sim 2 - 3$ . The higher densities and faster ionization rates tend to mitigate the effect of collisionless electron heating, favoring the convergence to the canonical  $\beta = \beta_{min}$  case (compare panels c of Figures 3 and 4).

Varying the value of  $\rho_{AM}$  has an immediate impact on the emission measures and emission measure averaged quantities, mainly through the hydrodynamic scaling laws mentioned in Paper I. The approximate scaling of  $EM_X(t)$  and  $\langle \tau \rangle_X(t)$  is given by eqs. (3)-(5) in Paper I:  $\rho_{AM}^{-1/3}$  for the t axis,  $\rho_{AM}$  for  $EM_X(t)$  and  $\rho_{AM}^{2/3}$  for  $\langle \tau \rangle_X(t)$ . These approximate scalings are accurate within a factor of 2 for  $2 \cdot 10^{-25} \leq \rho_{AM} \leq 5 \cdot 10^{-24} \text{g} \cdot \text{cm}^{-3}$ , but they might break down for values of  $\rho_{AM}$  outside this range. The effect of a change of  $\rho_{AM}$  on the electron temperatures is more complex, and difficult to approximate with sufficient accuracy in view of the sensitivity of X-ray spectra to electron temperature. Whereas an accuracy within a factor of 2 is reasonable for  $EM_X$  and  $\tau_X$ , which span several orders of magnitude, changes by a factor of 2 are too large compared with the more modest (but still up to 2 orders of magnitude) range in  $T_e$ .

## 2.4. Effects on the X-ray Spectrum

In Figure 5, the temporal evolution of the spectra from the shocked ejecta of model DDTe is presented for three values of  $\rho_{AM}$  ( $10^{-24}$ ,  $5 \cdot 10^{-24}$ , and  $2 \cdot 10^{-25} \text{g} \cdot \text{cm}^{-3}$ ) and two values of  $\beta$  ( $\beta_{min}$  and 0.1). A preliminary inspection reveals that variations in  $\rho_{AM}$  have profound effects on the calculated spectra. As expected from the scaling law for  $\langle \tau \rangle_X$ , the plasma ionization state varies greatly, and the presence of different ions results in emission of different ionic lines. At  $\rho_{AM} = 5 \cdot 10^{-24} \text{g} \cdot \text{cm}^{-3}$ , for instance, the more advanced ionization state of Fe leads to a higher flux in the Fe L complex, which blends with O Ly $\alpha$  and Mg He $\alpha$  emission at the *XMM-Newton* CCD spectral resolution. The increase in the Fe K $\alpha$  line,

on the other hand, is due to the higher temperatures in the ejecta. The prominent O He $\alpha$  line at 0.56 keV, seen at early times for  $\rho_{AM} = 10^{-24} \text{g} \cdot \text{cm}^{-3}$ , disappears at higher values of  $\rho_{AM}$ , because He-like O is ionized more rapidly. The overall higher ionization state of the plasma also leads to an increase in the flux of the Ly $\alpha$  lines of Si and S, and a shift towards higher energies of the Ca K $\alpha$  line. The shape and flux of the continuum emission also change. At lower densities, these effects are reversed. The Fe K $\alpha$  line and Fe L complex virtually disappear, revealing the underlying Ne He $\alpha$  and Ne Ly $\alpha$  lines at 0.9 and 1.0 keV. The O He $\alpha$  line becomes more important than O Ly $\alpha$ , and the Ly $\alpha$  and He $\beta$  lines of Si and S vanish almost completely, as well as the Ca K $\alpha$  line. The continuum flattens and the emitted flux is generally lower at all energies.

In contrast with the global effects of variations of  $\rho_{AM}$ , changes in the amount of collisionless heating at the reverse shock have a different impact on different elements in a model with stratified ejecta like DDTe. For  $\rho_{AM} = 10^{-24} \text{g} \cdot \text{cm}^{-3}$ , the flux in the Fe K $\alpha$  line, which probes material at higher  $T_e$  and lower  $\tau$  than the Fe L complex, is increased by almost two orders of magnitude for  $\beta = 0.1$ . None of the other elements seems to be affected at this AM density, although model DDTe has a significant amount of S, Si and Ca in the inner ejecta. This increase in the Fe K $\alpha$  flux becomes less pronounced with time, and is accompanied by a slight change in the shape of the continuum. For  $\rho_{AM} = 5 \cdot 10^{-24} \text{g} \cdot \text{cm}^{-3}$ , the continuum is unaffected and the increase of the Fe K $\alpha$  line flux is reduced to less than an order of magnitude at early times, disappearing completely at late times. At  $\rho_{AM} = 2 \cdot 10^{-25} \text{g} \cdot \text{cm}^{-3}$ , however, the collisionless electron heating has a more noticeable effect. The shape of the spectrum is not changed at low energies, but the flux is somewhat lower at early times for  $\beta = 0.1$ . At high energies, the level of continuum rises and the flux in the Fe K $\alpha$  line flux greatly increases. The effects of collisional electron heating can be clearly seen even at CCD spectral resolution. With a higher spectral resolution such as provided by *ASTRO-E2*, the predicted large temperature increases caused by collisionless heating (Fig. 2) should be detectable through various temperature-sensitive line diagnostics for a number of different chemical elements within the shocked ejecta.

We emphasize that model DDTe is presented here just as an illustrative example. For obvious reasons, it is not practical to present the effects of  $\rho_{AM}$  and  $\beta$  on the spectra of all the models in our grid. Although the details may vary, the general trends identified here for DDTe can be applied to most of the other models (for a discussion of other delayed detonation models, see Badenes et al. 2005).

To conclude, we note that collisionless electron heating at the reverse shock can have interesting effects on the spatially resolved X-ray emission. In particular, the enhanced flux in the Fe K $\alpha$  line discussed above would come mainly from the hotter regions of Fe-rich ejecta

close to the reverse shock (see the shape of the electron temperature profile in Figures 1, 3, and 4 for values of  $\beta$  above 0.01). This scenario is compatible, at least qualitatively, with the finding that the Fe  $K\alpha$  emission peaks at a smaller radius than the Fe L and Si He $\alpha$  emission in the X-ray CCD images of both the Tycho (Hwang et al. 1998) and Kepler (Cassam-Chenai et al. 2004) SNRs. Collisionless electron heating provides a simpler explanation to the rise of the electron temperature profile towards the reverse shock than the relic of an interaction with a circumstellar medium invoked by Dwarkadas & Chevalier (1998) for the Tycho SNR.

### 3. X-RAY SPECTRUM FROM THREE DIMENSIONAL TYPE Ia EXPLOSION MODELS

#### 3.1. Type Ia SN Explosions in 3D: Fundamental Properties

In Paper I, we introduced a grid of eight one dimensional Type Ia SN explosion models that included examples of all the paradigms currently under debate: sub-Chandrasekhar explosions, deflagrations, delayed detonations, and pulsating delayed detonations. This reduced grid is just a representative sample of a more extensive grid of 19 models, which constituted the base for the study of Type Ia SNRs conducted by Badenes (2004). The remaining 11 grid models are intermediate cases obtained by varying the parameters involved in the calculation of each explosion paradigm. We have included these models in the Appendix, both for reference in future works and for the convenience of those readers who want to use our synthetic SNR spectra for their own research. This grid is one representation of our current understanding of one dimensional Type Ia explosion models, upon which most of our knowledge of the physics of Type Ia SNe is based.

In view of the recent developments in the field, however, it has become clear that 1D calculations will soon be superseded by the three dimensional models that have begun to appear in the literature (Reinecke et al. 2002; Gamezo et al. 2003; Travaglio et al. 2004; García-Senz & Bravo 2005). These works have focused on pure deflagrations in 3D, proving that they are capable of producing robust explosions, but the ability of these models to explain the observations of Type Ia SNe has not been fully established yet. A common feature in all 3D deflagration models, and the most remarkable difference with respect to 1D models, is the uniform mixing of unburnt C and O material with  $^{56}\text{Ni}$  and the other products of nuclear burning throughout the ejecta. This mixing is due to the deformation of the flame front caused by Rayleigh-Taylor instabilities, an effect which seems unavoidable in 3D deflagrations. There has been some concern that the presence of large amounts of C and O in the inner layers of ejecta would lead to a spectral evolution inconsistent with optical observations (Gamezo et al. 2003), but complex spectral simulations are required to

verify this claim (Baron et al. 2003). Alternatives to the 3D deflagration scenario are being explored right now, including delayed detonations in 3D (García-Senz & Bravo 2003; Gamezo et al. 2004b,a) and two new explosion paradigms: gravitationally confined detonation (Plewa et al. 2004) and pulsating reverse detonation (Bravo et al. 2005), but none of these models has been completely understood yet. Here, we study 3D deflagration models in the context of the X-ray spectra of young SNRs to provide an independent method of assessing their viability for Type Ia explosions.

We use a one dimensional average of model B30U, a 3D deflagration from García-Senz & Bravo (2005), to illustrate what can be expected from this class of models. The chemical composition and density profile of this model are presented in the Appendix, and they are very similar to those of the models obtained by Gamezo et al. (2003) and Travaglio et al. (2004), even though the computational techniques and the resolution of the calculations are different in each case (see Table 1 in Bravo et al. 2005, for a more detailed comparison of these works). This shows that three dimensional deflagrations are relatively well understood, and supports our use of model B30U as a representative example of this class. The evolution of the emission measures and emission measure-averaged ionization timescales and electron temperatures of the principal elements in the ejecta of B30U are shown in Fig. 6 for an interaction with  $\rho_{AM} = 10^{-24} \text{g} \cdot \text{cm}^{-3}$  and  $\beta = \beta_{min}$ . Interpretation of differences between these plots and Figures 4, 5, and 6 of Paper I is not straightforward, because the 3D calculations are not fully self-consistent with the 1D models of the grid (the effect of the energy deposited by the decay of  $^{56}\text{Ni}$  on the density profile, for instance, has not been taken into account). Nevertheless, the main features of the evolution of the shocked ejecta do not depend on such details. The most striking property of this model is the similarity in the spectral properties ( $\langle T_e \rangle$  and  $\langle \tau \rangle$ ) of Fe and Si throughout the evolution of the SNR. This is in marked contrast to 1D models, where the stratification of the ejecta leads to significant differences between Fe and Si. The abrupt changes in several plots seen at  $t \sim 8 \cdot 10^{10}$  s are due to the impact of the reverse shock on a remnant of unburnt white dwarf material formed in model B30U (for details, see García-Senz & Bravo 2005).

In Figure 7, we show the ejecta spectra of model B30U at the same values of  $t$ ,  $\rho_{AM}$  and  $\beta$  as in Figure 5 for model DDTe. The most remarkable properties of these spectra are the high Fe L-shell flux and the presence of the prominent Ni  $K\alpha$  line at  $\sim 7.5$  keV (except at the lowest AM densities). This is due to the large amounts of Fe and Ni that are found in the outermost layers of B30U, where the density of the shocked ejecta is highest. The results are a long Fe ionization timescale, which leads to the enhanced Fe L-shell flux, and a high Ni emission measure leading to a strong Ni  $K\alpha$  emission. Such a strong Ni  $K\alpha$  line has never been observed in thermal X-ray spectra of SNRs. Another interesting feature is the relative weakness of the Si and S  $K\alpha$  lines. The reason for this is twofold: first, 3D

deflagrations produce smaller amounts of Si, S and other intermediate mass elements than the conventional 1D delayed detonations; second, equivalent widths of the Si and S lines are smaller because of the strong continuum produced by the large amount of C and O that is present throughout the ejecta. These spectral characteristics exhibited by model B30U are common to all 3D deflagrations with well mixed ejecta.

### 3.2. Comparison with X-ray observations of SNRs

We compare the results of our simulations for the 3D deflagration model B30U with the basic properties of Type Ia SNRs. The prediction of similar emission measure-averaged electron temperatures and ionization timescales for Si and Fe can be easily tested by examining X-ray observations. We have searched the literature for young SNRs with published good-quality X-ray spectra that have been classified as Type Ia. Six objects meet these requirements: the historical remnants of Tycho, Kepler and SN 1006, and three Large Magellanic Cloud SNRs: N103B, 0509-67.5, and DEM L71. We note that the classification of Kepler’s SNR as Type Ia is controversial (e.g., Blair 2004). The remnant of SN 1006 is not suitable for our purposes because it lacks strong Fe emission (Koyama et al. 1995). In the case of DEM L71, although the X-ray spectrum of this SNR has been analyzed in some detail (see Hughes et al. 2003; van der Heyden et al. 2003), we found no published estimates of temperatures and ionization timescales for Fe and Si in the ejecta. The results of the analysis of the integrated spectrum for the other four SNRs are summarized in Table 1.

The spectral properties of all the SNRs considered here show that an important fraction of the Fe in the shocked ejecta is emitting under conditions different from those of the Si. The authors of the works referenced in Table 1 accounted for this by either adding a spectral component made of pure Fe to their fits or by using plane-parallel models that allowed to treat Fe and Si separately by assigning different values of  $n_e t$  and  $kT$  to each element. Since the analysis techniques, models, and data quality were different in each case, these results can only be compared either with our models or among themselves in a qualitative way. Nevertheless, a clear trend can be observed in all four SNRs considered here: the Fe component was always hotter than the Si component by at least a factor of 2. The Fe was at a lower ionization timescale in three out of four objects: Tycho, Kepler, and N103B. In 0509-67.5, however, the Fe component has a higher ionization timescale than Si. In this case, the statistics of the Fe  $K\alpha$  line were poor, and the ionization timescale of Fe was constrained mostly by fitting the Fe L complex. Warren & Hughes (2004) note that their fit to the Fe L complex emission was not complete, because a strong line had to be added by hand. Improved atomic physics and higher resolution data would be highly desirable to confirm

this result for 0509-67.5.

Since the emission measure averaged ionization timescales and electron temperatures of Si and Fe do not differ by more than 30% in model B30U (see Figure 6), we conclude that this model is in conflict with the observations listed on Table 1, at least within the limitations of our simulations. This conclusion is extensible to any model in which Fe and Si are well mixed throughout the ejecta, and therefore can be applied to all the 3D deflagration models for Type Ia SNe discussed in the previous section. As we have seen in § 2, a plasma state with  $\langle T_e \rangle_{Si} < \langle T_e \rangle_{Fe}$  and  $\langle \tau \rangle_{Si} > \langle \tau \rangle_{Fe}$  arises naturally in Type Ia SN models with stratified ejecta, such as 1D delayed detonations or pulsating delayed detonations, that undergo a moderate amount of collisionless electron heating at the reverse shock. The ionization timescales of Fe and Si in 0509-67.5 are clearly incompatible with this scenario, but in this case Warren & Hughes (2004) found a very low amount of Fe in the shocked ejecta, with Fe to Si abundance ratios below 0.07. While this is very difficult to interpret in the context of well-mixed Type Ia SN ejecta, it could be more easily explained if the reverse shock were just entering the Fe-dominated region in stratified ejecta. A detailed comparison of our models with this SNR would be required to confirm this hypothesis.

We emphasize that our simulations based on one dimensional averages are too simple to rule out well-mixed 3D Type Ia SN explosion models. We do not account for a number of processes that might result in the Fe and Si in the ejecta emitting under different conditions, like the Ni bubble effect (Basko 1994; Blondin et al. 2001) or the formation of clumps in the ejecta (Wang & Chevalier 2001). Nevertheless, we find that the observations of Type Ia SNRs seem easier to explain in the light of Type Ia SN explosion models with stratified ejecta.

#### 4. DISCUSSION AND CONCLUSIONS

In this paper, we have examined several important aspects of the X-ray spectral models for the ejecta in Type Ia SNRs that were introduced in Badenes et al. (2003). We have explored the impact of the amount of collisionless electron heating at the reverse shock,  $\beta$ , and the density of the ambient medium,  $\rho_{AM}$ , on the integrated X-ray emission from the ejecta in Type Ia SNR models of different ages. We found that even small amounts of collisionless electron heating can modify the electron temperature profile inside the ejecta in a significant way, leading to a region of hot material at low ionization timescales close to the reverse shock. In the context of Type Ia SN explosion models with stratified ejecta, this modified temperature profile can affect the emission from the inner layers rich in Fe for a broad range of dynamical ages, increasing the flux in the Fe K $\alpha$  complex. This could

explain why the Fe  $K\alpha$  emission peaks at smaller radii than Fe L in both the Tycho (Hwang et al. 1998) and Kepler (Cassam-Chenai et al. 2004) SNRs. The density of the AM also has a strong impact on the X-ray emission from the ejecta. For higher values of  $\rho_{AM}$ , the SNR is in a more advanced evolutionary stage at a given age, and the ionization timescale of the shocked ejecta increases significantly. At lower values of  $\rho_{AM}$ , the ionization timescales decrease and the evolutionary stage is less advanced. We have provided approximate scaling laws to estimate these effects, and discussed their impact on specific emission lines and line complexes through an example.

We have also reviewed the fundamental properties of the recent deflagration models for Type Ia SNe calculated in 3D, and their performance in the context of the X-ray spectra of SNRs. Using our 1D simulation scheme, we have shown that the mixing of fuel and ashes throughout the ejecta, which is a common feature of these 3D explosion models, results in all the elements in the shocked ejecta of the SNR having very similar spectral characteristics. In particular, the emission measure averaged ionization timescales and electron temperatures of elements like Fe and Si are always very close to each other. This is in conflict with the observations of Type Ia SNRs in our Galaxy and the Magellanic Clouds, where the Fe and Si in the shocked ejecta are found to be emitting under different physical conditions. Within the limitations of our 1D simulation scheme, these observations are easier to explain with Type Ia explosion models that have stratified ejecta than with models that have well mixed ejecta like 3D deflagrations.

We believe that our models represent a significant improvement over current methods of analyzing and interpreting the X-ray emission from the shocked ejecta in SNRs. In order to facilitate the comparison between our models and observations, we have built a library of synthetic spectra, which is available from the authors upon request. This library is presented in the Appendix, where more Type Ia SN explosion models are introduced, and some aspects relevant to the comparison between the synthetic spectra and observations are discussed. A detailed example of this kind of comparison in the framework of the ejecta emission from the Tycho SNR will be the subject of a forthcoming paper (Badenes et al., in preparation).

We wish to thank Jack Hughes and Jessica Warren for detailed discussions concerning 0509-67.5. We also acknowledge conversations with Una Hwang and Martin Laming on several aspects of the research presented here. We are grateful to the anonymous referee for suggestions that helped to improve the quality of this manuscript. This research has been partially supported by the CIRIT and MCyT in Spain, through grants AYA2000-1785, AYA2001-2360, and AYA2002-04094-C03. CB would like to acknowledge support from GENCAT (grant 2000FI 00376) and IEEC in Barcelona, and from grant GO3-4066X from SAO at Rutgers. KJB is supported by NASA grant NAG 5-7153.

## A. A LIBRARY OF SYNTHETIC SPECTRA FOR THE ANALYSIS OF EJECTA EMISSION IN TYPE Ia SNRs

In this Appendix, we introduce our library of synthetic spectra for the ejecta emission in Type Ia SNRs. The objective of this library is to provide observers with a complete set of synthetic spectra for the ejecta emission in SNRs, calculated from an extensive grid of Type Ia SN explosion models, at different values of  $t$ ,  $\rho_{AM}$ , and  $\beta$ . At present, our library includes more than 800 synthetic spectra in sequences like those presented in Figures 5 and 7 for models DDTe and B30U. For each model, we have generated synthetic spectra for several values in the ranges  $430 \leq t \leq 5000$  yr;  $2 \cdot 10^{-25} \leq \rho_{AM} \leq 5 \cdot 10^{-24} \text{g} \cdot \text{cm}^{-3}$ ; and  $\beta_{min} \leq \beta \leq 0.1$ . In § A.1, we discuss these synthetic spectra in the context of the tools that are currently used for the analysis of ejecta emission in SNRs. In § A.2 we comment on potential applications for our models. In § A.3, some important caveats and limitations of the models are discussed. Finally, in § A.4, we introduce a number of Type Ia SN explosion models that, together with those presented in Paper I, complete the exploration of the parameter space for thermonuclear supernovae.

### A.1. Rationale

The spectral analysis of the ejecta emission in young SNRs is a complex problem. Despite the spectacular increase in the quality of the observations, it has proved very difficult to extract the relevant physical parameters from these observations in a reliable way with the available tools. A frequent approach involves the fitting of several more or less sophisticated NEI components with varying abundances, electron temperatures, and ionization timescales to the observed X-ray spectra (several examples have been cited in § 3.2). The results of applying this approach are not unique, and frequently very hard to interpret, because average parameters (like  $T_e$  or  $n_e t$ ) are assigned to a plasma whose physical properties have an enormous dynamic range, and where different chemical elements often emit under different conditions (see Figures 1, 3, and 4). The determination of elemental abundances in the entire volume of shocked plasma, which is crucial for establishing the connection between the SNRs and the SN explosions that originated them, is particularly unreliable when it is based on this approach. Often, NEI models just provide estimates for the emission measures of the elements, under the assumption of a homogeneous composition, and the difference between the ratios of these emission measures and the true abundance ratios in the plasma can be several orders of magnitude (see section 4.2 of Paper I).

The synthetic spectra presented in Paper I and in the present work open new possibilities for the interpretation of X-ray observations of Type Ia SNRs. Without claiming to include

all the complex physical processes at play in young SNRs (see § A.3), these synthetic spectra provide a much more accurate representation of the state of the shocked ejecta in young Type Ia SNRs than the simple NEI models currently available within software packages like XSPEC. Moreover, since the synthetic spectra are calculated from realistic SN explosion models, the connection between the observed spectrum and quantities like the explosion energy or the amount of each element present in the ejecta are easy to establish. The trade off is that the comparison between our synthetic spectra and X-ray observations is not necessarily a straightforward procedure.

## A.2. Comparing Models and Observations

Several strategies with varying degrees of sophistication can be followed to compare our models to observations. A somewhat crude possibility is to focus on derived quantities like  $\langle T_e \rangle$  and  $\langle \tau \rangle$ , as we have done in § 3.2. While this can lead to interesting results, it is far better to perform more direct spectral comparisons using the library of synthetic spectra that we present here. The most effective way to apply this library will depend on the specific observational constraints for the SNR under study. In some cases, like the historical Galactic SNRs, the age will be known accurately, but the distance (and hence the total integrated X-ray flux and the radius of the forward shock) will be more uncertain. In other cases, like the SNRs in the Magellanic Clouds, the distance will be known, but the age will not. Reliable independent estimates for  $\rho_{AM}$  may or may not be available. In each case, there will be more than one way to reduce the dimensionality of the problem. Rather than providing a recipe which may not be adequate for a specific case, we make here some suggestions which might prove useful in a more general context.

First, it is important to note that each synthetic spectrum is based on an underlying hydrodynamic model, so quantities such as the radius of the forward and the reverse shocks and their expansion parameters are available for each spectral model (see Figure 3 and eqns. (3), (4), and (5) in Paper I). In principle, it is possible to reverse the problem, find out which hydrodynamic models agree better with the observations and thus reduce the number of synthetic spectra to consider. In doing so, however, the limitations of 1D adiabatic hydrodynamics must be considered (see the following section). Second, the selection of a particular synthetic spectrum from our library to represent the ejecta component in an observed X-ray spectrum may not be trivial. The substantial uncertainties in the atomic data and the relative simplicity of the models with respect to real SNRs will probably make it impossible to attain a statistically valid fit. Synthetic spectra like ours are more vulnerable to these factors, because there is little room for self-adjustment, in contrast to conventional

NEI models with variable abundances. If the emissivity of a particular line is underestimated in the spectral code used to generate our library, for instance, this cannot be compensated by artificially enhancing the abundance of that particular element, as in a conventional NEI model. Yet, even if some specific details of the observed spectrum cannot be reproduced, it is often possible to find a model whose overall characteristics are in reasonable agreement with the observations. Under these circumstances, a procedure needs to be devised in order to measure the degree of success of a specific synthetic spectrum. An example shall be provided in a forthcoming paper on the Tycho SNR (Badenes et al., in preparation).

### A.3. Approximations and Caveats

Our models are just a simplified representation of the complexity of young SNRs, and their limitations have to be considered when making comparison with observations. The crucial approximations were reviewed in sections 3.5 and 5 of Paper I, but it is important to revisit several issues here.

The most important simplification is certainly the assumption of spherical symmetry. Any description of young SNRs in the framework of 1-D models is necessarily incomplete, because it does not include important processes such as ejecta clumping and dynamic instabilities at the contact discontinuity between shocked ejecta and shocked AM (Chevalier et al. 1992; Wang & Chevalier 2001). The degree of ejecta clumping is crucial, and it is clear that our 1D models (and in particular, the distribution of  $\tau$  and  $T_e$  for each element) would be invalidated if clumps with a large density contrast like those proposed by Wang & Chevalier (2001) were to dominate the emission measure of the shocked ejecta in Type Ia SNRs. In this case, gross inconsistencies are expected to emerge from comparison of 1-D models with observations. The degree of ejecta clumping strongly affects the morphology of the X-ray emission, and examination of this morphology in Type Ia SNRs should shed light on this issue. Multi-dimensional hydrodynamical simulations coupled with X-ray emission calculations could prove useful for this.

Another important issue whose impact on the X-ray spectra is hard to estimate is the effect of cosmic ray acceleration at the shocks. There is some indication that this process might affect the dynamics and X-ray spectra of the shocked AM without significantly modifying those of the shocked ejecta (Decourchelle et al. 2000), but more detailed simulations are needed to shed light on this question (see Ellison et al. 2005, for a discussion).

To conclude this section, we comment on the importance of radiative losses, which have received some attention lately in the work of Blinnikov et al. (see Blinnikov et al. 2004, and

references therein). In Section 4 of Hamilton & Sarazin (1984), it was shown that radiative losses always lead to catastrophic cooling in heavy element plasmas, driving the shocked material to infrared- and optically-emitting temperatures. Because no optically emitting knots with a composition dominated by heavy elements have been observed in Kepler, Tycho, or SN 1006 (see Blair et al. 1991; Smith et al. 1991), we conclude that radiative losses are not dynamically important in young Type Ia SNRs under usual conditions. Radiative losses are not included in our models in a self-consistent way, but we have extended the *a posteriori* monitoring of radiative losses described in section 3.5 of Paper I to the more unfavorable case of  $\rho_{AM} = 5 \cdot 10^{-24} \text{g} \cdot \text{cm}^{-3}$ . Our previous conclusions have been verified: radiative losses only affect the outermost layers of the models with the steepest ejecta density profiles. The values of  $t_{rad}$ , as defined in Paper I (the time when the calculated losses exceed 10% of the specific internal energy in at least 5% of the ejecta mass) for models with  $t_{rad} < 5,000$  yr are provided in Table 2. In these models, our calculations for the properties (density, electron temperature, ionization state, and X-ray emission) of the layers that undergo radiative losses are not reliable close to or beyond  $t_{rad}$ , and some amount of infrared or optical emission should be expected from this region of the ejecta. The fact that such emission is not observed in Kepler, Tycho or SN 1006 suggests that models which predict substantial radiative losses in the ejecta are in conflict with observations of these historical SNRs.

## A.4. The Complete Grid of Type Ia SN Explosion Models

### A.4.1. One Dimensional Models

Among the eight one dimensional Type Ia SN explosion models introduced in Paper I, one was a sub-Chandrasekhar explosion (SCH), one was a pure detonation (DET), two were pure deflagrations (DEFa and DEFf), two were delayed detonations (DDTa and DDTe), and two were pulsating delayed detonations (PDDa and PDDe). These explosion paradigms, and the details involved in the calculation of the models, are described in Paper I (Section 2 and Appendix). For the deflagrations, delayed detonations and pulsating delayed detonations, the models presented in Paper I were extreme cases, obtained by considering the highest and lowest reasonable values of the parameters involved in each calculation. In the case of the deflagration models, the relevant parameter is  $\kappa$ , which controls the propagation velocity of the subsonic flame. For the delayed detonation and pulsating delayed detonation, the parameters are  $\rho_{tr}$ , which determines the density at which the transition from deflagration to detonation occurs, and  $\iota$ , which determines the flame velocity in the deflagration stage. All these parameters are defined in the Appendix of Paper I. By varying these parameters, we have generated four more deflagrations (DEFb, DEFc, DEFd, and DEFe), four more delayed

detonations (DDTb, DDTbb, DDTc, and DDTd), and three more pulsating delayed detonations (PDDb, PDDc, and PDDd). In Table 3 and Figure 8, we present the nucleosynthetic output, chemical composition profiles and density profiles of these intermediate models that complete the exploration of the parameter space.

#### *A.4.2. Three Dimensional Models*

A brief discussion on the state of the art in 3D calculations of thermonuclear SN explosions can be found in § 3.1 of this work; for a review see Bravo et al. (2005). Without going into the details of how these 3D models are calculated, here we present four one-dimensional mappings of 3D models that are representative of the current trends. Their main characteristics are given in Figure 8 and Table 4. Model B30U is a 3D deflagration from García-Senz & Bravo (2005), very similar to the models by Gamezo et al. (2003) and Travaglio et al. (2004) (see discussion in § 3). Model DDT3DA is a 3D version of the delayed detonation paradigm (García-Senz & Bravo 2003). In this model, a detonation was artificially inducted in those regions where the flame resulting from the turbulent deflagration phase was well described by a fractal surface of dimension larger than 2.5. We note that this particular model also results in very well mixed ejecta, and in fact the properties of its X-ray emission in the SNR phase are very similar to those of model B30U. Other delayed detonations in 3D calculated with different assumptions for the induction of the detonation result in more stratified ejecta (Gamezo et al. 2004b,a). For a comparison between these two kinds of three dimensional delayed detonations, see Table 1 and the accompanying text in Bravo et al. (2005). Finally, two 3D sub-Chandrasekhar models from García-Senz et al. (1999) have also been included in the grid. Model SCH3DOP is a sub-Chandrasekhar explosion calculated in 3D where the layer of degenerate He was ignited at one single point, while in SCH3DMP the ignition happened at five different points. It is worth noting that none of the 3D models has been followed for a sufficient time to account for the effects of the decay of  $^{56}\text{Ni}$  on the density profiles.

## REFERENCES

- Badenes, C. 2004, PhD thesis, Universitat Politècnica de Catalunya
- Badenes, C., Bravo, E., Borkowski, K., & Domínguez, I. 2003, *ApJ*, 593, 358 [Paper I]
- Badenes, C., Bravo, E. & Borkowski, K. 2005, *Adv. Space Res.*, submitted
- Baron, E., Lentz, E., & Hauschildt, P. 2003, *ApJ*, 588, L29
- Basko, M. 1994, *ApJ*, 425, 264
- Blair, W. 2004, in 1604-2004: Supernovae as Cosmological Lighthouses, ed. M. Turatto, L. Zampieri, S. Benetti, & W. Shea. (ASP Conference Series), in press [astro-ph/0410081]
- Blair, W., Long, K., & Vancura, O. 1991, *ApJ*, 366, 484
- Blinnikov, S., Bakalanov, P., A.V.Kozyreva, & Sorokina, E. 2004, in 1604-2004: Supernovae as Cosmological Lighthouses, ed. M. Turatto, L. Zampieri, S. Benetti, & W. Shea. (ASP Conference Series), in press [astro-ph/0409396]
- Blondin, J., Borkowski, K., & Reynolds, S. 2001, *ApJ*, 557, 782
- Borkowski, K., Lyerly, W., & Reynolds, S. 2001, *ApJ*, 548, 820
- Branch, D. & Khokhlov, A. 1995, *Phys. Rep.*, 256, 53
- Bravo, E., Badenes, C. & García-Senz, D. 2005, in *Interacting Binaries: Accretion, Evolution and Outcomes*, ed. L.A. Antonelli, L. Burderi, F. D’Antona, T. Di Salvo, G.L. Israel, L. Piersanti, O. Straniero & A. Tornambé. (AIP Conference Series), in press, [astro-ph/0412155]
- Cargill, P. & Papadopoulos, K. 1988, *ApJ*, 329, L29
- Cassam-Chenai, G., Decourchelle, A., Ballet, J., Hwang, U., Hughes, J., & R.Petre. 2004, *A&A*, 414, 545
- Chevalier, R. 1982, *ApJ*, 258, 790
- Chevalier, R., Blondin, J., & Emmering, R. 1992, *ApJ*, 392, 118
- Decourchelle, A., Ellison, D., & Ballet, J. 2000, *ApJ*, 543, L57
- Dwarkadas, V. & Chevalier, R. 1998, *ApJ*, 497, 807

- Ellison, D., Decourchelle, A., & Ballet, J. 2005, *A&A*, 429, 569
- Gamezo, V., Khokhlov, A. & Oran, E. 2005, *ApJ*, submitted [astro-ph/0409598]
- Gamezo, V., Khokhlov, A. & Oran, E. 2004, *Phys. Rev. Lett.*, 92, 1102
- Gamezo, V., Khokhlov, A., Oran, E., Chtchelkanova, A., & Rosenberg, R. 2003, *Science*, 299, 77
- García-Senz, D. & Bravo, E. 2003, in *From Twilight to Highlight: The Physics of Supernovae*, ed. W. Hillebrandt and B. Leibundgut (Berlin: Springer), 158 [astro-ph/0211242]
- García-Senz, D. & Bravo, E. 2005, *A&A*, in press, [astro-ph/0409480]
- García-Senz, D., Bravo, E. & Woosley, S. E. 1999, *A&A*, 349, 177
- Ghavamian, P., Raymond, J., Smith, R., & Hartigan, P. 2001, *ApJ*, 547, 995
- Hamilton, A. & Fesen, R. 1988, *ApJ*, 327, 178
- Hamilton, A., Fesen, R., Wu, C., Crenshaw, D., & Sarazin, C. L. 1997, *ApJ*, 481, 838
- Hamilton, A. & Sarazin, C. 1984, *ApJ*, 287, 282
- Hillebrandt, W. & Niemeyer, J. 2000, *ARA&A*, 38, 191
- Höflich, P. & Khokhlov, A. 1996, *ApJ*, 457, 500
- Hughes, J., Ghavamian, P., Rakowski, C., & Slane, P. 2003, *ApJ*, 582, L95
- Hughes, J., Hayashi, I., Helfand, D., Hwang, U., Itoh, M., Kirshner, R., Koyama, K., Markert, T., Tsunemi, H., & Woo, J. 1995, *ApJ*, 444, L81
- Hwang, U., Hughes, J., & Petre, R. 1998, *ApJ*, 497, 833
- Kinugasa, K. & Tsunemi, H. 1999, *PASJ*, 51, 239
- Koyama, K., Petre, R., Gotthelf, E., Hwang, U., Matsuura, M., Ozaki, M., & Holt, S. 1995, *Nature*, 378, 255
- Laming, J. M. 2000, *ApJS*, 127, 409
- Lewis, K., Burrows, D., Hughes, J., Slane, P., Garmire, G., & Nousek, J. 2003, *ApJ*, 582, 770
- Plewa, T., Calder, A.C., & Lamb, D.Q. 2004, *ApJ*, 612, L37

- Rakowski, C., Ghavamian, P., & Hughes, J. 2003, *ApJ*, 590, 846
- Reinecke, M., Hillebrandt, W., & Niemeyer, J. 2002, *A&A*, 391, 1167
- Smith, R., Kirshner, R., Blair, W., & Winkler, P. 1991, *ApJ*, 375, 652
- Travaglio, C., Hillebrandt, W., Reinecke, M., & Thielemann, F.-K. 2004, *A&A*, 425, 1029
- van der Heyden, K., Bleeker, J., Kaastra, J., & Vink, J. 2003, *A&A*, 406, 141
- Vink, J., Laming, M., Gu, M., Rasmussen, A., & Kaastra, J. 2003, *ApJ*, 587, L31
- Wang, C.-Y. & Chevalier, R. 2001, *ApJ*, 549, 1119
- Warren, J. & Hughes, J. 2004, *ApJ*, 608, 261

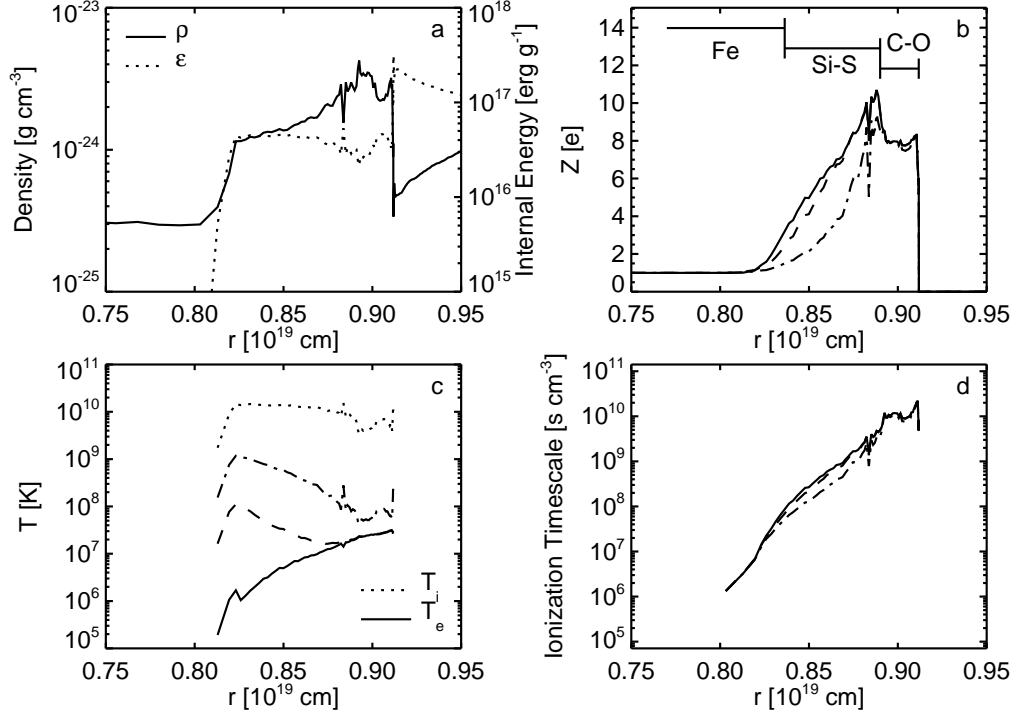


Fig. 1.— Shoked ejecta structure vs. radius for model DDTe interacting with an ambient medium of density  $10^{-24} \text{ g} \cdot \text{cm}^{-3}$ , 430 years after the explosion. The panels show the radial distribution of density and specific internal energy (a), mean number of electrons per ion,  $\bar{Z}$ , with an indication of the ejecta layers dominated by Fe, Si-S and C-O (b), electron and ion temperatures (c) and ionization timescale (d). The positions of the reverse shock and contact discontinuity are outlined by the limits of the temperature plots in panel c. The three plots for  $\bar{Z}$  (panel b),  $T_e$  (panel c) and  $\tau$  (panel d) represent the values obtained with  $\beta = \beta_{min}$  (solid),  $\beta = 0.01$  (dashed) and  $\beta = 0.1$  (dash-dotted).

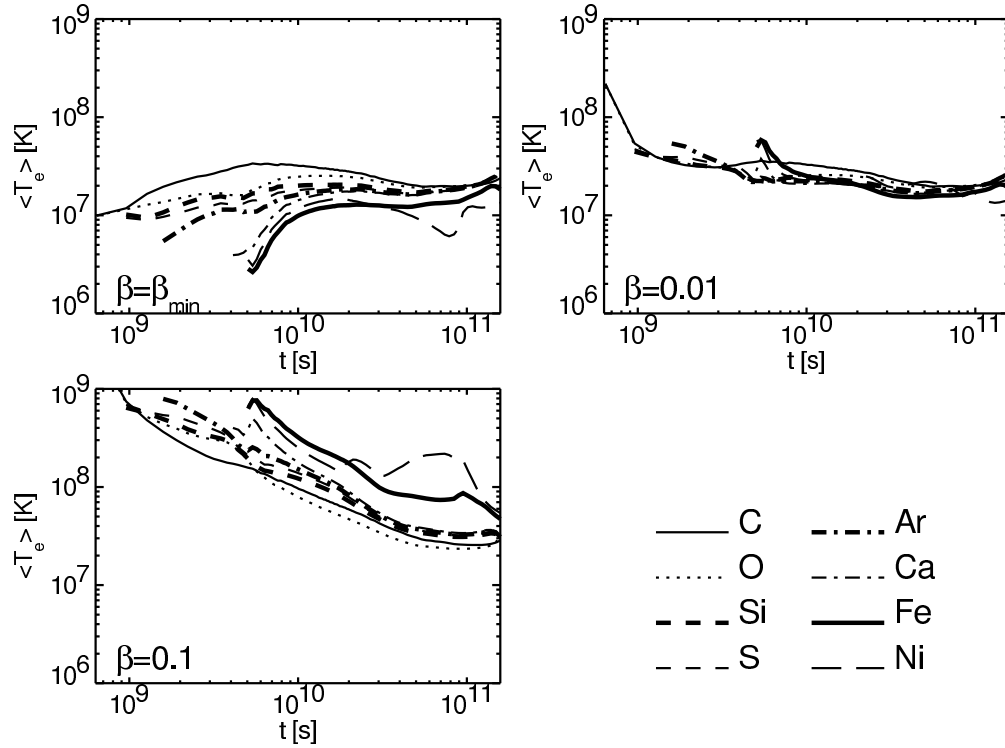


Fig. 2.— Evolution of  $\langle T_e \rangle_X$  for C, O, Si, S, Ar, Ca, Fe and Ni in the shocked ejecta of model DDTe, with  $\rho_{AM} = 10^{-24} \text{ g} \cdot \text{cm}^{-3}$ . The top left panel corresponds to  $\beta = \beta_{min}$ , and is the same as panel b of Figure 5 in Paper I, but with a different scale. The top right panel corresponds to  $\beta = 0.01$ , and the bottom left panel to  $\beta = 0.1$ .

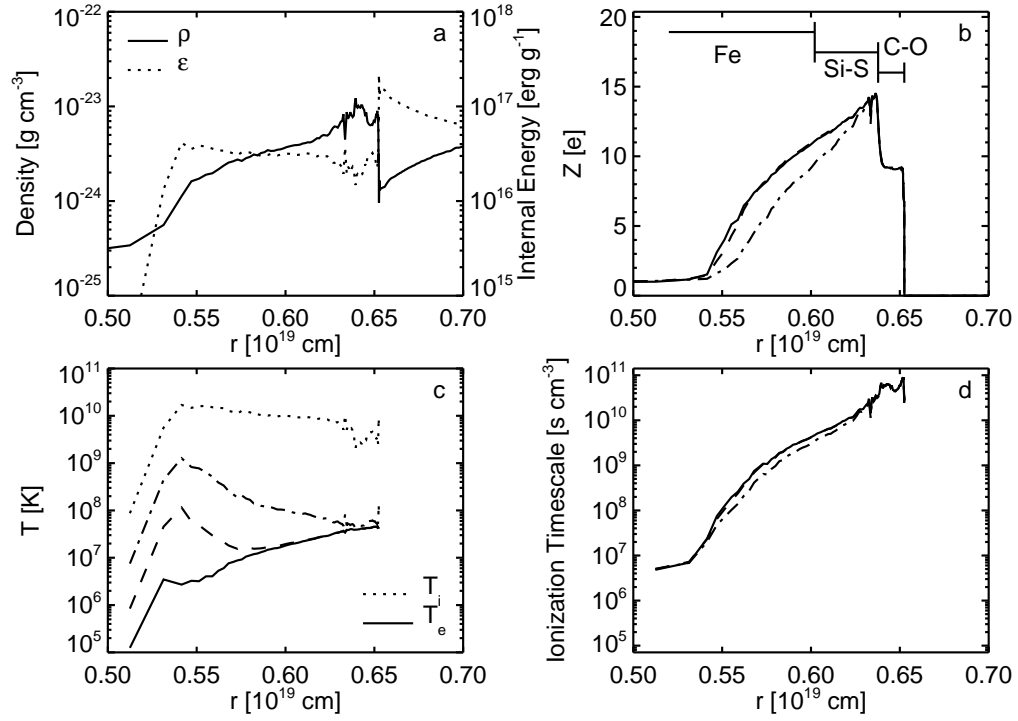


Fig. 3.— Shoked ejecta structure vs. radius for model DDTe, with  $\rho_{AM} = 5 \cdot 10^{-24} \text{ g} \cdot \text{cm}^{-3}$ , 430 years after the explosion. See Figure 1 for an explanation of the plots and labels.

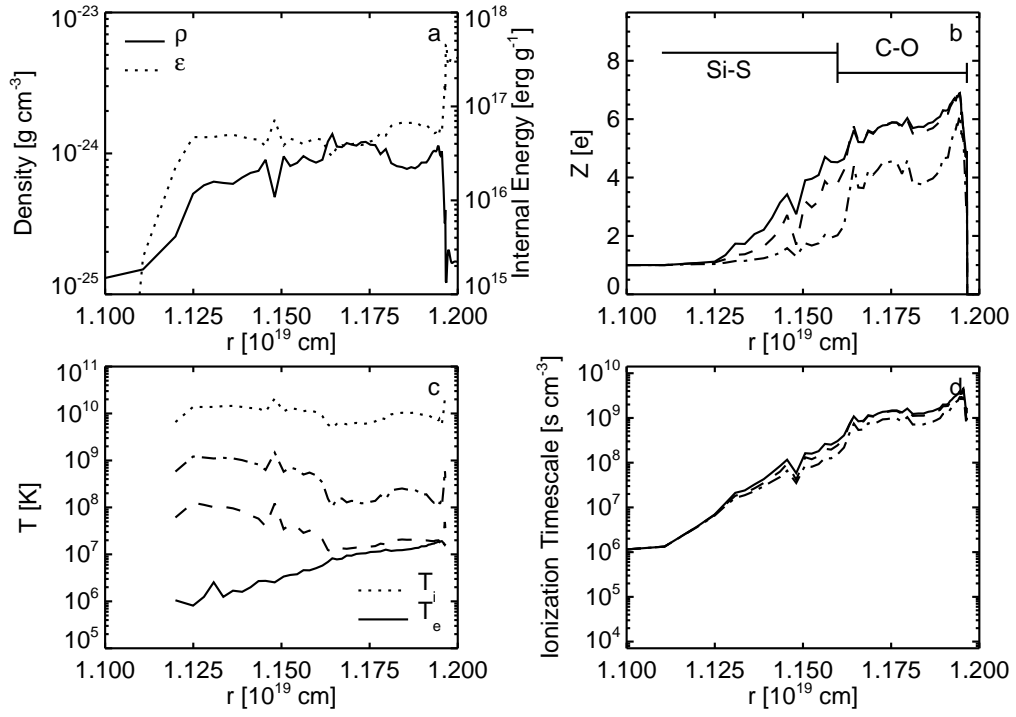


Fig. 4.— Shoked ejecta structure vs. radius for model DDTe, with  $\rho_{AM} = 2 \cdot 10^{-25} \text{ g} \cdot \text{cm}^{-3}$ , 430 years after the explosion. See Figure 1 for an explanation of the plots and labels.

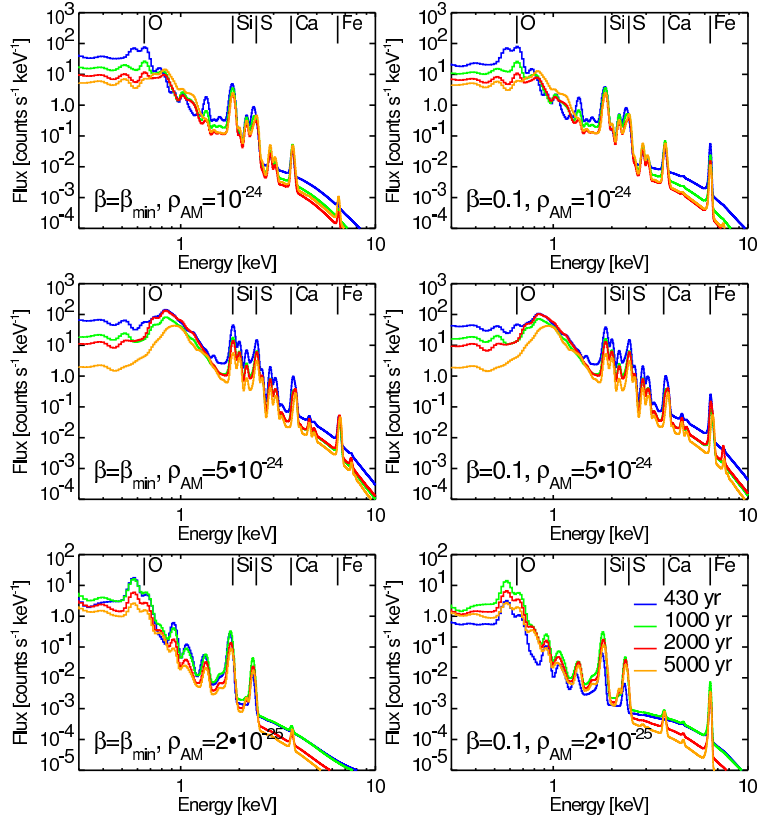


Fig. 5.— Unabsorbed X-ray spectra from the shocked ejecta of the DDTe model, 430, 1000, 2000 and 5000 yr after the SN explosion, for  $\rho_{AM} = 10^{-24} \text{g} \cdot \text{cm}^{-3}$  (top panels),  $5 \cdot 10^{-24} \text{g} \cdot \text{cm}^{-3}$  (middle panels), and  $2 \cdot 10^{-25} \text{g} \cdot \text{cm}^{-3}$  (bottom panels), convolved with the spectral response of the *XMM-Newton* EPIC MOS1 CCD camera. The spectra in the left panels correspond to  $\beta = \beta_{min}$ , those in the right panels to  $\beta = 0.1$ . The  $K\alpha$  lines of Fe, Ca, S, and Si, as well as the O  $Ly\alpha$  line, have been marked for clarity, and fluxes are calculated at a fiducial distance of 10 kpc. Note that the spectral code has no atomic data for Ar. See the on-line edition for a color version of this Figure.

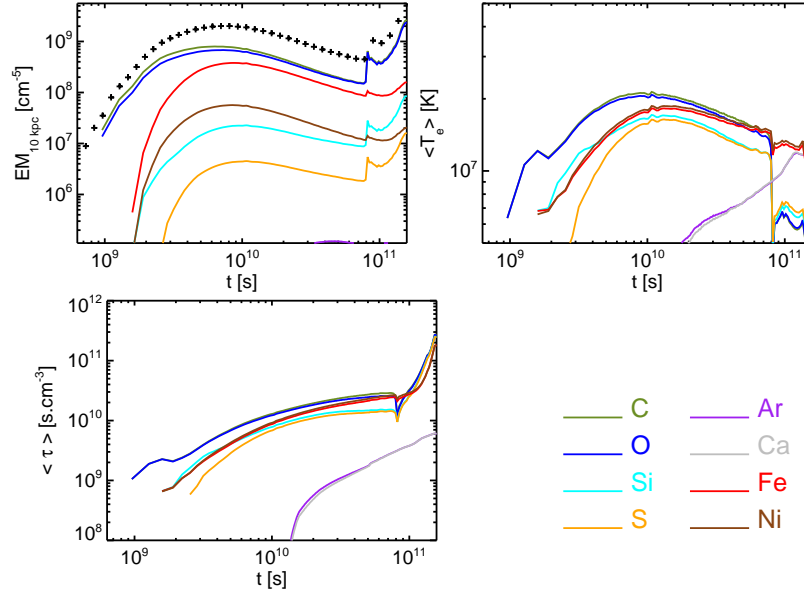


Fig. 6.—  $EM(t)$  (top left),  $\langle T_e \rangle (t)$  (top right) and  $\langle \tau \rangle (t)$  (bottom) for the principal elements in the shocked ejecta of model B30U, interacting with a uniform AM of  $\rho_{AM} = 10^{-24} \text{g} \cdot \text{cm}^{-3}$ . The crosses in the  $EM(t)$  plot represent the total emission measure of the shocked ejecta. See the on-line edition for a color version of this Figure.

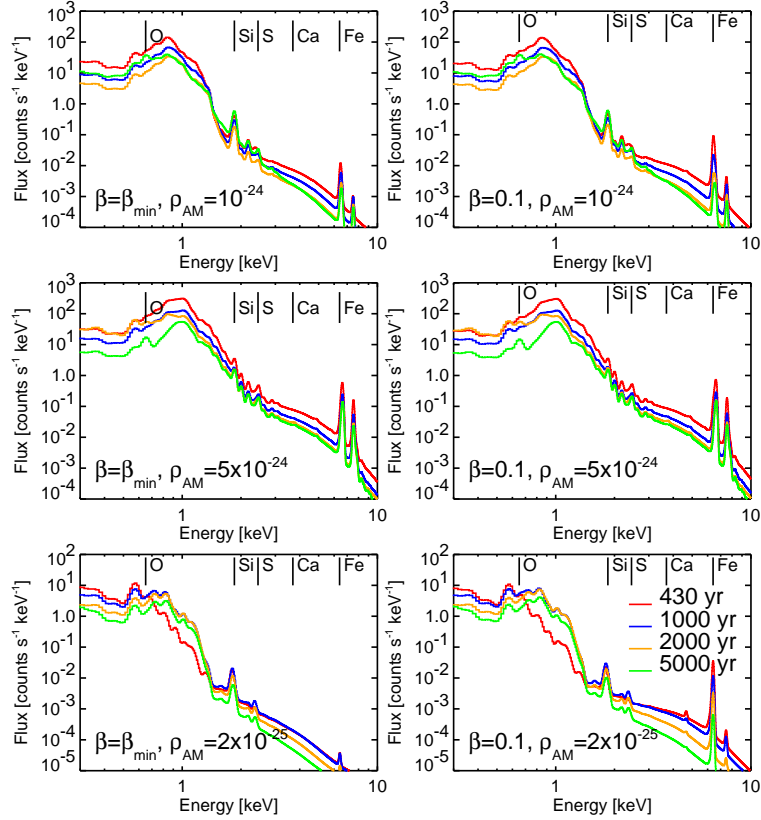


Fig. 7.— Unabsorbed X-ray spectra from the shocked ejecta in the B30U model, 430, 1000, 2000 and 5000 yr after the SN explosion, for  $\rho_{AM} = 10^{-24} \text{g} \cdot \text{cm}^{-3}$  (top panels),  $5 \cdot 10^{-24} \text{g} \cdot \text{cm}^{-3}$  (middle panels), and  $2 \cdot 10^{-25} \text{g} \cdot \text{cm}^{-3}$  (bottom panels). The spectra in the left panels correspond to  $\beta = \beta_{min}$ , those in the right panels to  $\beta = 0.1$ . See Figure 5 for an explanation of the labels and plots. The online edition of the journal contains a color version of this Figure.

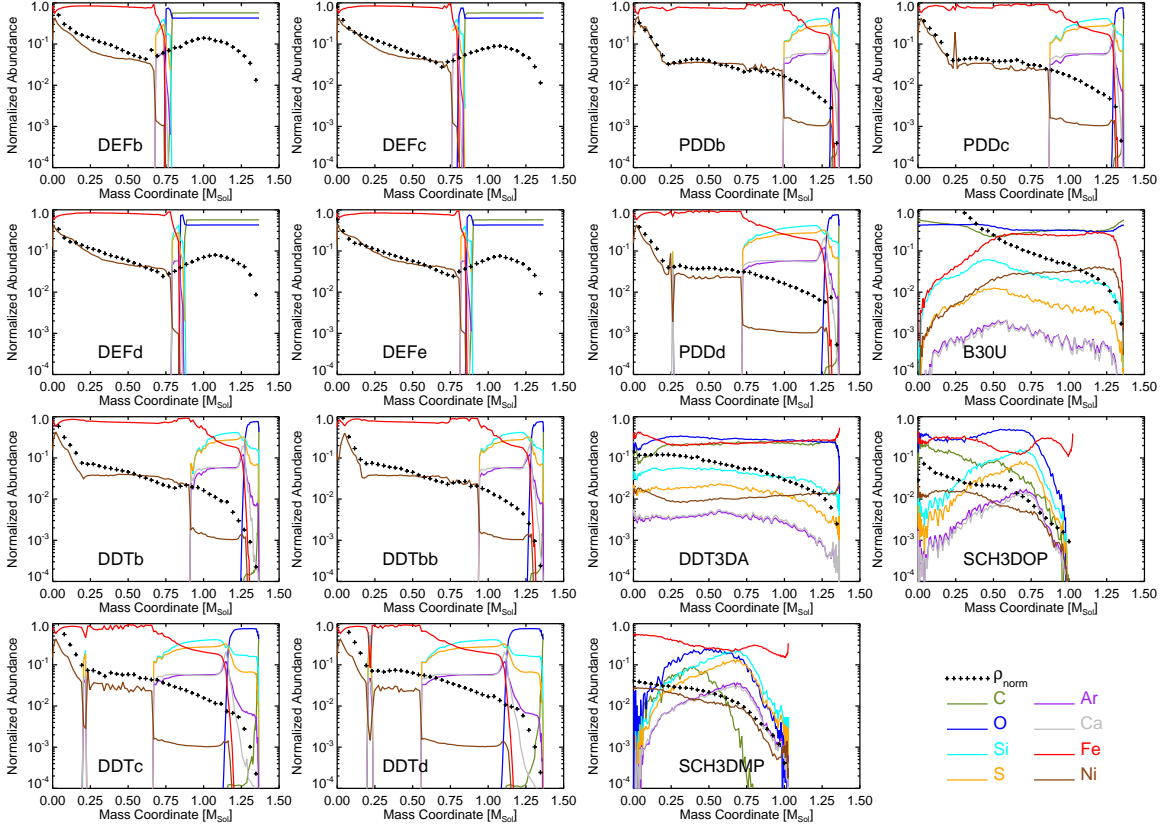


Fig. 8.— Chemical composition and density profiles for the Type Ia SN explosion models that were not presented in Paper I. The abundances represented here are number abundances after the decay of all short lifetime isotopes. The density profiles ( $\rho_{norm}$ ) are represented at  $t = 10^6$  s after the SN explosion, and they have been normalized by  $\rho_n = 10^{-11} \text{ g} \cdot \text{cm}^{-3}$ . See the on-line edition for a color version of this Figure.

Table 1. Spectral properties of Fe and Si in Type Ia SNRs

SNR	Reference	Age [yr]	Si component <sup>a</sup>			Fe component		
			Spectral model	$kT$ [keV]	$\log n_e t$ [cm <sup>3</sup> s]	Spectral model	$kT$ [keV]	$\log n_e t$ [cm <sup>3</sup> s]
Tycho	Hwang et al. (1998)	432	NEI, single $T_e$ , single $n_e t$	0.86	$\sim 11$	NEI, single $T_e$ , single $n_e t$	$> 1.7$	$\sim 9$
Kepler <sup>b</sup>	Kinugasa & Tsunemi (1999)	404	NEI, single $T_e$ , single $n_e t$ <sup>c</sup>	$0.77 \pm 0.06$	$10.42^{+0.06}_{-0.05}$	NEI, single $T_e$ , single $n_e t$ <sup>c</sup>	$> 6$	$9.53^{+0.07}_{-0.01}$
0509-67.5	Warren & Hughes (2004)	$< 1,000$	Plane-parallel NEI shock <sup>d</sup>	$3.13 \pm 0.55$	$9.93 \pm 0.02$	Plane-parallel NEI shock <sup>d</sup>	$10.0^{+\infty}_{-5.44}$	$10.53 \pm 0.02$
N103B	Lewis et al. (2003)	$< 2,000$ <sup>e</sup>	Plane-parallel NEI shock	$\sim 1$	$> 12$	Plane-parallel NEI shock	$> 2$	$\sim 10.8$

<sup>a</sup>In all the cases listed here, the 'Si component' also included some Fe, as well as other elements.

<sup>b</sup>The identification of this SNR as Type Ia is controversial, see Blair (2004).

<sup>c</sup>Kinugasa & Tsunemi (1999) also fitted the spectrum with an NEI component for the Fe  $K\alpha$  line plus a more sophisticated model for the rest of the shocked ejecta and AM, based on the self-similar solutions of Chevalier (1982), coupled to NEI calculations in a plasma with homogeneous abundances. However, they do not give explicit values for  $kT$  and  $n_e t$  of the reverse shock in this model. For simplicity, we use the results of their two-component NEI model, which gives a fit of similar quality.

<sup>d</sup>We list the results for the best fit model in Warren & Hughes (2004), which includes a nonthermal continuum (their model S). Assuming a thermal continuum (their model H), these authors obtain similar results:  $kT_{Si} = 2.23 \pm 0.29$ ,  $\log n_e t_{Si} = 9.94 \pm 0.02$ ,  $kT_{Fe} = 10.00^{+\infty}_{-4.14}$ ,  $\log n_e t_{Fe} = 10.53 \pm 0.02$ .

<sup>e</sup>Hughes et al. (1995).

Table 2. Values of  $t_{rad}$  <sup>a</sup>

Model	$\rho_{AM} = 10^{-24} \text{g} \cdot \text{cm}^{-3}$	$\rho_{AM} = 5 \cdot 10^{-24} \text{g} \cdot \text{cm}^{-3}$
DEFa	$3.0 \cdot 10^{10} \text{ s}$	$2 \cdot 10^{10} \text{ s}$
DEFc	$2.7 \cdot 10^{10} \text{ s}$	$1.6 \cdot 10^{10} \text{ s}$
DEFf	$2.4 \cdot 10^{10} \text{ s}$	$1.2 \cdot 10^{10} \text{ s}$
PDDe	-	$1.5 \cdot 10^{11} \text{ s}$

<sup>a</sup>Only models with  $t_{rad} < 5,000 \text{ yr}$  ( $1.58 \cdot 10^{11} \text{ s}$ ) are listed. The values of  $t_{rad}$  for other DEF models (DEFb, DEFd and DEFe) are comparable. All calculations were done with  $\beta = \beta_{min}$

Table 3. Properties of the additional Type Ia 1D explosion models

Model	Para- meter <sup>a</sup>	$\rho_{tr}$ [g · cm <sup>-3</sup> ]	$M_{ejecta}$ [M <sub>⊙</sub> ]	$E_k$ [10 <sup>51</sup> erg]	$\mathcal{M}_{max}$ <sup>b</sup> [mag]	$\Delta\mathcal{M}_{15}$ <sup>b</sup> [mag]	$M_{Fe}$ [M <sub>⊙</sub> ]	$M_{C+O}$ [M <sub>⊙</sub> ]	$M_{Si}$ [M <sub>⊙</sub> ]	$M_S$ [M <sub>⊙</sub> ]	$M_{Ar}$ [M <sub>⊙</sub> ]	$M_{Ca}$ [M <sub>⊙</sub> ]
DEFb	0.08		1.37	0.64	-19.14	0.94	0.61	0.61	0.025	0.017	0.0040	0.0043
DEFc	0.10		1.37	0.74	-19.29	0.99	0.68	0.55	0.021	0.014	0.0032	0.0032
DEFd	0.12		1.37	0.80	-19.34	1.02	0.71	0.52	0.021	0.014	0.0032	0.0034
DEFe	0.14		1.37	0.81	-19.29	0.98	0.73	0.49	0.021	0.013	0.0029	0.0028
DDTb	0.03	$2.6 \cdot 10^7$	1.37	1.36	-19.67	1.11	0.98	0.05	0.10	0.084	0.022	0.027
DDTbb	0.01	$2.5 \cdot 10^7$	1.37	1.31	-19.66	1.12	0.99	0.05	0.10	0.084	0.022	0.027
DDTc	0.03	$2.2 \cdot 10^7$	1.37	1.16	-19.51	1.11	0.80	0.12	0.17	0.13	0.033	0.038
DDTd	0.03	$1.5 \cdot 10^7$	1.37	1.08	-19.30	0.94	0.72	0.14	0.20	0.15	0.037	0.043
PDDb	0.03	$2.2 \cdot 10^7$	1.37	1.36	-19.72	1.14	1.04	0.03	0.085	0.070	0.018	0.022
PDDc	0.03	$1.5 \cdot 10^7$	1.37	1.25	-19.64	1.11	0.98	0.04	0.11	0.093	0.024	0.029
PDDd	0.03	$1.2 \cdot 10^7$	1.37	1.24	-19.53	1.04	0.89	0.05	0.15	0.13	0.034	0.041

<sup>a</sup>The parameter given is  $\kappa$  for the DEF models and  $\iota$  for the DDT and PDD models (see the Appendix of Paper I for details).

<sup>b</sup>The values of  $\mathcal{M}_{max}$  and  $\Delta\mathcal{M}_{15}$  for the light curves were calculated by I. Domínguez (private communication, 2003).

Table 4. Properties of the 3D Type Ia explosion models

Model	$M_{ejecta}$ [ $M_{\odot}$ ]	$E_k$ [ $10^{51}$ erg]	$M_{Fe}$ [ $M_{\odot}$ ]	$M_{C+O}$ [ $M_{\odot}$ ]	$M_{Si}$ [ $M_{\odot}$ ]	$M_S$ [ $M_{\odot}$ ]	$M_{Ar}$ [ $M_{\odot}$ ]	$M_{Ca}$ [ $M_{\odot}$ ]
B30U	1.37	0.42	0.53	0.66	0.045	0.011	0.0019	0.0017
DDT3Da	1.37	0.78	0.76	0.38	0.063	0.027	0.0066	0.0072
SCH3DOP	1.02	1.14	0.58	0.23	0.064	0.035	0.0093	0.0077
SCH3DMP	1.02	1.19	0.67	0.07	0.081	0.054	0.019	0.017